

Accepted for the publication in the *Astrophysical Journal*

Spatial Variation of the X-ray spectrum of the Crab Nebula

Koji Mori and David N. Burrows

*Department of Astronomy and Astrophysics, Pennsylvania State University, 525 Davey
Laboratory, University Park, PA. 16802, USA*

mori@astro.psu.edu

J. Jeff Hester

*Department of Physics and Astronomy, Box 871504, Arizona State University, Tyler Mall,
Tempe, AZ. 85287-1504, USA*

George G. Pavlov

*Department of Astronomy and Astrophysics, Pennsylvania State University, 525 Davey
Laboratory, University Park, PA. 16802, USA*

Shinpei Shibata

Department of Physics, Yamagata University, Yamagata 990-8560, Japan

and

Hiroshi Tsunemi

*Department of Earth and Space Science, Graduate School of Science, Osaka University, 1-1
Machikaneyama, Toyonaka, Osaka 560-0043, Japan*

ABSTRACT

We present spectral analysis of the Crab Nebula obtained with the *Chandra* X-ray observatory. The X-ray spectrum is characterized by a power-law whose index varies across the nebula. The variation can be discussed in terms of the particle injection from the pulsar in two different directions: the equatorial plane containing the torus and the symmetry axis along the jet. In the equatorial plane, spectra within the torus are the hardest, with photon index $\alpha \approx 1.9$, and are almost independent of the surface brightness. At the periphery of the torus,

the spectrum gradually softens in the outer, lower surface brightness regions, up to $\alpha \approx 3.0$. This indicates that synchrotron losses become significant to X-ray emitting particles at the outer boundary of the torus. We discuss the nature of the torus, incorporating information from observations at other wavelengths. Spectral variations are also seen within the southern jet. The core of the jet is the hardest with $\alpha \approx 2.0$, and the outer sheath surrounding the core becomes softer with α up to 2.5 at the outermost part. Based on the similarity between the spectra of the jet core and the torus, we suggest that the electron spectra of the particles injected from the pulsar are also similar in these two different directions. The brightness ratio between the near and far sides of the torus can be explained by Doppler boosting and relativistic aberration; however, the observed ratio cannot be derived from the standard weakly magnetized pulsar wind model. We also found a site where an optical filament comprised of supernova ejecta is absorbing the soft X-ray emission (< 2 keV).

Subject headings: ISM: individual (Crab Nebula) — supernova remnants — X-rays: ISM

1. INTRODUCTION

The observed pulsating radiation is only a small fraction of a pulsar’s spin-down energy. The bulk of this energy is carried off in the form of a magnetized, relativistic pulsar wind. This pulsar wind is randomized by a shock where its pressure balances that of the ambient material (Rees & Gunn 1974; Kennel & Coroniti 1984). Diffuse synchrotron radiation is expected to arise from the randomized pulsar wind, forming a *pulsar wind nebula* (PWN). Although this general idea is widely accepted, details of the formation are still controversial. For example, it is a long-standing problem that the ratio of the Poynting flux to the particle kinetic flux just upstream of the shock, σ , is much smaller than 10^{-2} , in spite of expectations that the ratio at the light cylinder is larger than unity (e.g., Arons 2002). Additionally, the formation of the torus and the collimation of the pulsar wind to form a jet along the rotational axis are quite curious but unresolved problems.

An X-ray observation is a powerful probe to peer into the inner PWN, whose spectral and morphological properties provide essential information to answer such questions. Recent *Chandra* and *XMM-Newton* observations increased the number of objects where spatially resolved X-ray spectroscopy within the PWN can be performed. In a number of PWNe, the spectrum of the outer edges of the PWN is observed to be softer than the spectrum of the center (e.g., G21.5–0.9, Slane et al. 2000, Safi-Harb et al. 2001; 3C 58, Bocchino et al. 2001;

G0.9+0.1, Porquet et al. 2003; G54.1+0.3, Lu et al. 2002; Vela, Kargaltsev & Pavlov 2004). Since the synchrotron energy losses are proportional to the square of the particle energy, the higher energy particles have shorter life times and the spectrum becomes softer as they move down the post-shock flow, which is in general agreement with these observations. Such spatial variation of the spectrum can be used to verify theoretical models and to provide new diagnostics for the study of PWNe.

The Crab Nebula has been one of the best examples for investigating a PWN. Its X-ray brightness and large apparent structure including the torus (Aschenbach & Brinkmann 1975) and jets (Brinkmann, Aschenbach, & Langmeier 1985) make it an ideal target for spatially resolved X-ray spectroscopy. Previous *Chandra* and *XMM-Newton* observations have also shown spectral softening of the Crab (Weisskopf et al. 2000; Willingale et al. 2001). Here, we present spectral analysis results from multiple observations of the Crab Nebula with the Advanced CCD Imaging Spectrometer (ACIS) on board *Chandra*, which are derived from the monitoring program described by Hester et al. (2002).

2. OBSERVATION AND ANALYSIS

Owing to the X-ray brilliance of the Crab Nebula, observations with the *Chandra* ACIS instrument are technically challenging. The high count rate generally causes two problems in the data acquisition: telemetry saturation and event pile-up (caused by more than one photon depositing charge in a given pixel during a CCD exposure, thereby compromising our ability to measure the energy of each individual photon). Although telemetry saturation results in loss of observing efficiency, it does not lead to biased estimates of physical parameters (e.g., count rate) because events are discarded in a unit of frames, not event by event. On the other hand, pile-up makes interpretation of spectral results problematic, since it converts two photons into a single “event” which has apparent energy equal to the sum of the photon energies. This results in underestimated count rate and hardens the detected spectrum, as discussed in Weisskopf et al. (2000).

We observed the Crab Nebula eight times (Table 1), using an instrumental mode of ACIS-S different from that of Weisskopf et al. (2000) in order to reduce pile-up. We adopted a frame time of 0.2 sec instead of the standard frame time of 3.2 seconds, but we did not utilize the grating to reduce count rate. This reduced the counts pixel⁻¹ frame⁻¹ by a factor of 2.3 with respect to the data of Weisskopf et al. (2000), while improving statistics by increasing the total number of counts by one order of magnitude for a similar effective exposure time. Since the Crab Nebula is a diffuse source, the event pile-up was suppressed by more than a factor of 2.3. The observational parameters (e.g., telemetry format of graded

mode, no dithering) were the same through the eight observations. A combined image from the last seven observations is shown in Figure 1a (the first observation did not include the whole remnant due to an instrument setup error). This image is an order of magnitude deeper than the image of Weisskopf et al. (2000).

In order to study X-ray spectral variations within the Crab Nebula, we divided the whole image into $2''.5 \times 2''.5$ square regions, from which spectra were extracted. The eight data sets were combined in the analysis in order to provide each region with enough statistics. We excluded regions dominated by scattered photons (less than 2000 counts per analysis region) and/or by trailing (or “out of time”) events. Trailing events, which are caused by photons detected during the CCD readout, can be seen not only as the line emanating from the pulsar along the detector readout direction (which is almost east-west for all of our observations), but also as diffuse emission which dominates the faint regions to the east and west of the nebula due to the enormous brilliance of the Crab PWN. The number of the trailing events in a given pixel can be estimated by multiplying the total number of events integrated along the readout direction by the ratio of the charge transfer row period to the frame exposure time (this ratio is 1.89×10^{-4}). We exclude regions where more than 20% of the total events recorded in that region are due to the trailing events.

We fitted the 2074 spectra with a power-law model in the 0.5–8 keV energy band. We included galactic absorption with a fixed N_{H} of $3.2 \times 10^{21} \text{cm}^{-2}$, which is derived from a fit of the faintest region where pile-up is negligible. The recently discovered quantum efficiency decay of ACIS¹ is taken into account². Figure 2a shows a correlation plot of apparent photon index versus observed surface brightness. The statistical errors of the apparent photon indices are quite small. They can be roughly expressed empirically as $0.01 \times I^{-0.5}$ where I is the observed surface brightness in unit of $\text{counts s}^{-1} \text{arcsecond}^{-2}$ (90% confidence level).

In spite of the reduction in counts per frame, many of the spectra are still distorted by event pile-up. The spectral parameters derived from a fit of the whole nebula spectrum with a power-law plus galactic absorption model are summarized in Table 2 (uncorrected values), as are the canonical values for comparison. The pile-up results in a lower apparent spectral index and lower apparent intensity than the canonical values. The observed intensity normalization is about 84% of that estimated from the canonical values with the instrumental response. Pile-up has the effect of reducing photon index in regions of increased surface brightness, which is the same general trend seen in the data of Figure 2a. The pile-up effects must be corrected in order to determine the nature of any real spectral variations across the

¹See <http://asc.harvard.edu/cal/Acis/Cal.prods/qeDeg/index.html>

²See <http://www.astro.psu.edu/users/chartas/xcontdir/xcont.html>

Crab nebula.

In order to estimate how pile-up distorts the incident spectrum, we utilized the spectral simulator tool LYNX (Chartas et al. 2000). LYNX traces the propagation of individual photons through the mirror and ACIS via the raytrace tool MARX (Wise et al. 1997) and the PSU ACIS Monte Carlo CCD simulator (Townsend et al. 2001), respectively. Since LYNX takes into account the possible overlap of the resulting charge clouds within each CCD exposure frame, spectra affected by pile-up can be simulated for both point sources and diffuse sources. We simulated the observed Crab spectrum for several different values of true surface brightness and for true photon indices of 1.5, 2.0, and 2.5. The results are superposed on the data in Figure 2a. The expected reduction of apparent photon index in higher surface brightness regions is evident. However, it is also clear that the variations in observed photon indices greatly exceed those expected from pile-up, and there are certainly real spectral variations across the Crab Nebula, as described by Weisskopf et al. (2000).

We used the LYNX simulation results to correct the data points in Figure 2a for the photon index and surface brightness errors induced by the pile-up effects. For each data point, we interpolated the simulated data points to the observed surface brightness and photon index and calculated the corresponding true surface brightness and photon index. Figure 2b presents a correlation plot of the corrected data points. This simulation was intended to give corrections on the data points in Figure 2a and was not adjusted to correct the whole nebula spectrum in order to match to the canonical spectral parameters. However, we used the corrected photon indices and surface brightnesses of each data point in Figure 2b to calculate a corrected spectrum for the whole nebula and we present the results in Table 2 (corrected values). The photon index and the normalization factor of the corrected spectrum agree well with the canonical values within the errors, which strongly supports the success of our pile-up corrections. Hereafter, we use the terms “photon index” and “surface brightness” to mean these corrected values.

We should note a limitation of our simulation. Our corrections are based on modeling of a uniform diffuse source. We apply them to each $2''.5 \times 2''.5$ square region under the reasonable assumption that the surface brightness within each region is uniform. Therefore, application of this technique to small complicated structures like the inner ring or the relativistically expanding wisps requires more complex modeling which is beyond the scope of this work. The systematic errors of the photon index mainly come from this assumption. Judging from the results of the simulation shown in Figure 2a and typical surface brightness fluctuations of $\sim 10\%$ within an analysis region, the systematic errors in photon index are ~ 0.05 and dominate the statistical errors.

Figure 1b shows a map of the photon index. The structure in the torus is more sym-

metrical about the pulsar in the photon index map than in the broad-band image (Fig. 1a). While Doppler boosting and relativistic aberration brighten the northwestern portion of the torus (Pelling et al. 1987) in the Figure 1a image, by contrast there is relatively little variation of the photon index within the torus. The hardest structures in the nebula, with photon indices as low as 1.8, are the inner ring and portions of the torus, including the circular structures seen at each extremity of the torus discovered in the first *Chandra* observation (Weisskopf et al. 2000). However, these regions contain small complex structures and the hardest photon index should be re-examined using data set free from pile-up. The entire torus is quite hard ($\alpha \approx 1.9$) compared with the outer portions of the nebula. The southern jet is also relatively hard ($\alpha \approx 2.0$), whereas the northern counter jet is significantly softer ($\alpha \approx 2.25$). The bright region around the counter jet to the northwest of the torus, hereafter called the “umbrella” because of its shape, has even softer emission ($\alpha \approx 2.5$). Photon indices as large as 3.0 are found in the outer peripheral portions of the nebula.

3. RESULTS

We studied the spatial variation of the photon index over the nebula. As a first step, we divided the nebula into four prominent regions: the torus, the umbrella, the jet, and the peripheral region. We took the torus region as an ellipse bounding the far side of the torus. We also added two circles at each extremity of the ellipse to include the circular structures in the torus region. The rest of the bright nebula was taken as the umbrella region. The jet region covers only the southern jet. The peripheral region includes the faint emission surrounding the torus and umbrella regions except for the jet. Figure 3 shows that those four regions occupy separate regions in the plot of photon index against surface brightness, with the umbrella region significantly overlapping the torus and periphery. The color coding is shown in the inset figure.

The data points of the region within the torus (red) form a band with nearly constant photon index of ≈ 1.9 over a wide range of surface brightness (more than a factor of 4). Although the spectral index increases slightly for surface brightness below $0.4 \text{ counts s}^{-1} \text{ arcsecond}^{-2}$, this result shows that our spectral corrections were successful in removing the spectral distortion due to pile-up.

The data points of the peripheral region (green) dominate the low surface brightness / high photon index region. The photon indices at the periphery of the bright nebula are strongly anticorrelated to the surface brightness, even after correcting for pile-up effects. This makes a marked contrast to the constancy of the photon index in the torus, especially considering that the variation of the surface brightness in the periphery is $1/3$ of that in the

torus.

The photon indices of the jet (blue) are generally small compared to those of the peripheral regions although their surface brightnesses are comparable. The jet also shows a strong anticorrelation between surface brightness and photon index, again suggesting softening of the underlying electron spectrum at the boundaries of the jet.

The remaining population corresponds to the umbrella region (yellow). Although distributed over a similar wide range of surface brightness, the photon indices in the umbrella are generally greater than those of the torus region. In fact, the umbrella and torus merge both spatially and spectrally. The umbrella is seen only at the northern part of the nebula and has no counterpart with similar brightness in the south, where the jet is much more distinct.

4. DISCUSSION

4.1. Photon Index Variation

We found photon index variations across the nebula on arcsecond scales which are similar to those reported by Weisskopf et al. (2000) and Willingale et al. (2001) on larger angular scales. The photon index variations should be discussed along the two different directions of particle injection from the pulsar: the direction in the equatorial plane containing the torus, and the direction of the jet along the symmetry axis. We first consider the equatorial plane.

Although the standard model of the Crab Nebula given by Kennel and Coroniti (1984) assumes a spherical symmetry, it can be adapted to regions of limited solid angle in the equatorial plane. Across the equatorial plane, the spectrum is almost constant to the outer boundary of the torus, but softens significantly beyond this boundary. In the standard picture, the outer boundary of the torus is interpreted as a synchrotron burn-off boundary where the synchrotron losses become significant to the X-ray emitting particles. Until the outward post-shock flow reaches the torus, the synchrotron critical energy, E_c , must be greater than 10 keV and falls outside the *Chandra* X-ray band (0.5–8 keV). Here, the synchrotron critical energy is defined as the energy at which a spectral break occurs in the power-law spectrum.

Due to the shorter synchrotron life time of higher energy particles, the value of E_c for a given flow element decreases with time, hence with distance from the shock. Kennel and Coroniti (1984) gave E_c as a function of radius from the pulsar and explained the energy dependence of the overall nebular extent from optical to hard X-ray (~ 60 keV). In this picture, if the outer boundary of the X-ray torus is where the synchrotron burn-off

takes place in the X-ray band, then, in the same manner, larger tori are expected in the optical and radio bands. However, it is remarkable that the size of the torus does not change significantly over a wide bandpass. Optical images clearly show the torus and related circular structures with the same size as the X-ray images, albeit with less contrast (Hester et al. 2002). Temporal variations between two radio images taken 2 months apart also revealed a torus-like elliptical structure of the same size (Bietenholz et al. 2001). In hard X-ray images (22–43keV and 43–64keV; Pelling et al. 1987), again the nebular extent is similar to that of the torus seen in the soft X-ray band, in contradiction to an expectation that they should be smaller. Additionally, Shibata et al. (2003) showed that the observed surface brightness decreases as a function of distance beyond the torus much faster than expected from the Kennel & Coroniti model. Therefore, we suggest that the torus seen from radio to hard X-rays is not a simple result of synchrotron burn-off in a radial post-shock flow. The standard Kennel & Coroniti flow solution should be modified to include the torus structure observed in common over the wide bandpass. Detailed small-scale comparison of the synchrotron burn-off boundary between the X-ray and optical bands will reveal the true nature of the torus, which is the subject of a subsequent paper.

Figure 4 shows a close-up view of the photon index map around the southern jet. It shows that the spectral softening occurs from the central core of the jet, with $\approx \alpha$ of 2.0, to the outer fainter sheath regions, with $\approx \alpha$ of 2.5. Considering the cylindrical structure of the jet, the observed spectrum of the jet core is integrated through this structure and includes contributions from the softer outer sheath regions. The true photon index of the jet core is therefore even harder than 2.0, and must be close to that seen within the torus. Willingale et al. (2001), using *XMM-Newton*, reported that the jet has a spectrum steeper than the torus by 0.3, implying that the corresponding electron spectra differ by 0.6. However, this conclusion is based on the spectrum integrated all over the jet. The similarity of the jet core spectrum to that of the torus indicates that the electron spectra are actually rather similar in the two different directions of particle injection from the pulsar. This may give a strong constraint on theoretical models of magnetic collimation.

We estimate the fraction of the X-ray luminosity that comes from the jets as $\sim 4\%$, with $\sim 3\%$ from the southern jet and $\sim 1\%$ from the counter jet. The bright umbrella makes it difficult to estimate the luminosity from the counter jet and results in a relatively large uncertainty in its luminosity, although the discussion here is little affected. The jet luminosity fraction is close to the ratio of the volumes of the jets and the torus,

$$\frac{2 \int_0^{R_j} \int_0^{\theta_j} \int_0^{2\pi} r^2 \sin \theta \, dr \, d\theta \, d\phi}{\int_0^{R_t} \int_{\frac{\pi}{2}-\theta_t}^{\frac{\pi}{2}+\theta_t} \int_0^{2\pi} r^2 \sin \theta \, dr \, d\theta \, d\phi} = \frac{1 - \cos \theta_j}{\sin \theta_t} \left(\frac{R_j}{R_t} \right)^3, \quad (1)$$

where R_t , R_j , θ_t and θ_j are the radii and semi-opening angles of the torus and the jet. From Figure 1a, we see that $R_t \approx R_j$ and that θ_t and θ_j are 12° and 8° , respectively. Then, Equation (1) gives a ratio of about 5% for these volumes. Considering the uncertainties in the opening angles and model assumptions, the fraction of the total X-ray luminosity in the jet is comparable to its volume fraction, indicating that the volume emissivities of the jet and the torus are similar, even though they represent orthogonally different directions of particle injection from the pulsar. Taking $R_t = R_j = 50$ arcseconds ($\simeq 0.5$ pc assuming the distance of 2 kpc to the Crab Nebula) in the above equation (see Fig. 1a) and an X-ray luminosity in the 0.5–8 keV band of 1.3×10^{37} erg s $^{-1}$, which is estimated from the canonical spectral parameters, we obtain an average volume emissivity of $\sim 4 \times 10^{-18}$ erg s $^{-1}$ cm $^{-3}$.

4.2. Surface Brightness Ratio between Near and Far Sides of the Torus

The north-western (NW) part of the torus, which is the near side, is much brighter than the south-eastern (SE) part. The post-shock flows in the NW and SE parts are relativistically approaching and receding from us, respectively. Therefore, those apparent surface brightnesses are subject to Doppler boosting and relativistic aberration. Considering these effects, the surface brightness ratio of the NW part to the SE part should be given by

$$\left(\frac{1 + \beta \cos \theta}{1 - \beta \cos \theta} \right)^{\alpha+2}, \quad (2)$$

where θ is the angle measured in the observer’s frame between the direction of the flow and the line of sight, α is the photon index, and β is the flow speed at the torus normalized to the speed of light (Rybicki & Lightman 1979).

Hester et al. (2002) showed that the inner ring, which is inside the torus, is highly variable and that wisps moving at about $0.5c$ are emerging from the inner ring. This provides strong evidence that the inner ring represents the pulsar wind termination shock, whereas the torus is a downstream structure. Since the post-shock flow is sub-sonic, the flow speed decreases as a function of distance. Hester et al. (2002) and Mori (2002) showed that the *projected* speed of the far side of the torus is $0.03c$ – $0.1c$, measured directly east of the pulsar. The relatively large uncertainty is due to the small angular displacement of the far side of the torus. Considering relativistic effects and the geometry of the torus, where the rotational-symmetry axis lies about 58° west of north and about 25° out of the celestial plane, these speeds correspond to *true* speeds of $0.07c$ – $0.25c$ ($0.15c$). The value in parentheses is calculated for the central value of the *projected* speed range, $0.065c$. With $\alpha = 1.9$, these values should result in a surface brightness ratio of 1.6–6.3 (2.9). The observed surface

brightness ratio in Figure 1a is about 3.4, which agrees with the speed range inferred from above discussion.

Kennel & Coroniti (1984) deduced the post-shock flow speed as a function of z , the distance from the pulsar normalized to the shock radius, for different values of the magnetization parameter σ , the ratio of the Poynting flux to the particle kinetic flux upstream of the shock. From Figure 1a, z is about 2.7 at the distance where we measured the speed of the torus. Kennel & Coroniti suggested that σ is about 0.003 based on theoretical arguments, which would correspond to a velocity of about $0.05c$ at the torus (from Fig. 3 of Kennel & Coroniti), far below our measured value. Shibata et al. (2003) constructed a two-dimensional model image of the Crab Nebula in the framework of the Kennel & Coroniti model, and found that the model surface brightness ratio between the near and far sides of the torus is about 1.3 for $\sigma = 0.003$, also much lower than the observed value. By contrast, our measured speed of $0.07c$ – $0.25c$ ($0.15c$), which predicts the correct surface brightness ratio, corresponds to $\sigma = 0.01$ – 0.13 (0.05). The theoretical speed and brightness ratio values can be reconciled with the measured ones if we assume a σ of about 0.05.

It is worth noting that departures from spherical symmetry and proper treatment of radiative losses in the flow can both affect this result. It is likely that the flow is confined to a narrow range of latitudes around the equatorial plane upstream of the shock (the inner ring). After the shock the flow diverges out of the plane more rapidly than a radial flow to form the broad torus. This should result in more rapid deceleration than in a spherical model. Any radiative losses of particle pressure may also lead to greater compression and hence more rapid deceleration. In both cases, however, we might expect flow velocities *slower* than those predicted by Kennel & Coroniti, for a given σ . As a result, either of these effects could require an even greater σ to account for the observations.

4.3. Correlation between Column Density and Ejecta

There are some regions exhibiting unusually small photon index in Figure 3, which are enclosed by the red dashed circle. The corresponding positions in the nebula are shown in black in the inset, also enclosed by a red dashed circle. Figure 5 presents two spectra extracted from one of the small photon index regions and its neighboring region. The spectra are identical above about 2 keV, and the comparison of the spectra clearly reveals that the small apparent photon index is actually caused by a deficit of soft emission due to increased absorption in this region. Refitting the spectra from those regions with N_{H} treated as a free parameter, we obtained a similar photon index and a higher N_{H} , by $\sim 7 \times 10^{20} \text{ cm}^{-2}$, compared to the neighboring region.

The Crab Nebula appears to contain a number of embedded filaments in optical narrow-band emission-line images (e.g., Sankrit & Hester 1997). The optical filaments are thought to be the result of a Rayleigh-Taylor instability between the light pulsar wind nebula and the dense ejecta of the supernova explosion (Hester et al. 1996). The J2000 position of the region showing higher N_{H} , $\alpha = 05^{\text{h}}34^{\text{m}}29^{\text{s}}.6$, $\delta = +22^{\circ}00'30''.4$, coincides with knotty structure in the most prominent optical filament, which is often referred to as part of the “High-Helium Band” (MacAlpine et al. 1989). The emission lines from the High-Helium Band are blueshifted, indicating that this filament is located between the synchrotron nebula and us. In an optical continuum image, the knotty structure is visible as a “shadow” because it consists of dense dust which absorbs the optical synchrotron continuum from the PWN (e.g., Blair et al. 1997). Similarly, the higher N_{H} we find is likely due to absorption of soft X-rays by the dust and gas in this knotty structure. Assuming that the thickness of this filament is $5''$ based on the optical emission line images (Blair et al. 1997), which corresponds to $\sim 1.5 \times 10^{17}$ cm, the density of this filament corresponding to the observed X-ray absorption column density is $\sim 5 \times 10^3 \text{ cm}^{-3}$. The excess absorption can be seen only around the knotty structures all through this filament.

We searched for other examples of X-ray absorption from the “shadow” features in the optical continuum image (Hester et al. in preparation), from which we can pick up only dense dust core in filaments on the near side of the nebula. There are only a few such shadows within the X-ray nebula. The number of corresponding analysis regions is about 10 out of 2074 (in addition to the regions discussed above). The second noticeable shadows are located to the east of the pulsar, overlapping the edge of the torus. Excess absorption was again observed, but the amount was $\sim 3 \times 10^{20} \text{ cm}^{-2}$. The excess absorption related to other shadows is similar or less. Therefore, our results are little affected by soft X-ray absorption due to the filaments.

It is conceivable that our results are affected by intrinsic column density variation due to not only the optical filaments but also arcsecond scale variation of galactic absorption. We assessed this effect as follows. In Figure 3, the photon indices of the data points of the torus (red) having surface brightness higher than $0.5 \text{ counts s}^{-1} \text{ arcsec}^{-2}$ are distributed around the mean of 1.91 with the root mean square of 0.07. The statistical errors are small, so the observed scatter is dominated by systematic errors and by real variations in the power law index. We can obtain an upper limit on possible absorption variations across the nebula if we assume that this scatter is produced by variations in N_{H} , leading to an estimate of the variation in N_{H} of $2 \times 10^{20} \text{ cm}^{-2}$.

5. SUMMARY

We have shown spatial variations of the X-ray spectrum of the Crab Nebula in terms of photon index, at an angular scale of arcseconds. The variations can be viewed in two different directions of the particle injection from the pulsar.

Across the equatorial plane, the spectrum is almost constant to the outer boundary of the torus, with photon index $\alpha \approx 1.9$ regardless of the surface brightness. It softens significantly, up to $\alpha \approx 3.0$, in the outer, fainter peripheral region. This seems qualitatively consistent with the previous suggestions that the outer boundary of the torus is interpreted as a synchrotron burn-off boundary where the synchrotron losses become significant to X-ray emitting particles. However, the fact that structures similar to the torus are seen at other wavelengths indicates that the torus is not a simple result of synchrotron burn-off.

Within the southern jet, photon index variations are also seen: the spectral softening takes place from the central core to the outer sheath. The photon index at the central core is almost the same as that of the torus. This indicates that the electron spectra are similar in the two different directions of the particle injection from the pulsar. We also found that the volume emissivities of the jet and the torus are similar.

Assuming that the brightness difference between the near and far sides of the torus is caused by Doppler boosting and relativistic aberration, the ratio can be explained by the observed speed of the downstream flow at the torus. However it cannot be obtained from the so-called weakly magnetized pulsar wind with $\sigma \approx 0.003$, as suggested by Kennel & Coroniti (1984).

Finally, we found that an optical filament comprised of supernova ejecta surrounding the pulsar wind nebula is absorbing the soft X-ray emission from a small portion of the X-ray nebula.

The authors thank G. Chartas for his extensive cooperation on simulation using LYNX. We also thank the anonymous referee for comments which significantly improved the final text of this paper. K. M. acknowledges the support of JSPS through the fellowship for research abroad. The work of G. G. P. was partially supported by NASA grant NAG5-10865. This work was supported by the NASA through Chandra Awards G00-1032B and G01-2076B, issued by the Chandra X-ray Observatory Center, which is operated by the Smithsonian Astrophysical Observatory for and on behalf of NASA under contract NAS8-39073.

REFERENCES

- Aschenbach, B., & Brinkmann, W. 1975, *A&A*, 41, 147
- Arons, J. 2002, in *Neutron Stars in Supernova Remnants*, ed. P. O. Slane & B. M. Gaensler, (San Francisco: ASP), 71
- Blair, W. P., Davidson, K., Fesen, R. A., Uomoto, A., MacAlpine, G. M., & Henry, R. B. C. 1997, *ApJS*, 109, 473
- Brinkmann, W., Aschenbach, B., & Langmeier, A. 1985, *Nature*, 313, 662
- Chartas, G., Worrall, D. M., Birkinshaw, M., et al. 2000, *ApJ*, 542, 655
- Bietenholz, M. F., Frail, D. A., & Hester, J. J. 2001, *ApJ*, 560, 254
- Bocchino, F., Warwick, R. S., Marty, P., Lumb, D., Becker, W., & Pigot, C. 2001, *A&A*, 369, 1078
- Hester, J. J., Stone, J. M., Scowen, P. A., et al. 1996, *ApJ*, 456, 225
- Hester, J. J., Mori, K., Burrows, D. N. et al. 2002, *ApJ*, 577, L49
- Kargaltsev, O. & Pavlov, G. G. 2004, in *Young Neutron Stars and Their Environments*, IAU Symposium 218, ASP Conference Proceedings, eds F. Camilo and B. M. Gaensler, in press (astro-ph/0310767)
- Kennel, C. F., & Coroniti, F. V. 1984, *ApJ*, 283, 694
- Kuiper, L., Hermsen, W., Cusumano, G., Diehl, R., Schnfelder, V., Strong, A., Bennett, K., McConnell, M. L. 2001, *A&A*, 378, 918
- Lu, F. J., Wang, Q. D., Aschenbach, B., Durouchoux, P., & Song, L. M. 2002, *ApJ*, 568, L49
- MacAlpine, G. M., McGaugh, S. S., Mazzarella, J. M., & Uomoto, A. 1989, *ApJ*, 342, 364
- Mori, K. 2002, PhD thesis, Osaka University
- Pelling, R. M., Paciesas, W. S., Peterson, L. E., Makishima, K., Oda, M., Ogawara, Y., & Miyamoto, S. 1987, *ApJ*, 319, 416
- Porquet, D., Decourchelle, A., & Warwick, R. S. 2003, *A&A*, 401, 197
- Rees, M. J., & Gunn, J. E. 1974, *MNRAS*, 167, 1

- Rybicki, G. B., & Lightman, A. P. 1979, *Radiative Process in Astrophysics* (New York: Wiley-Interscience)
- Safi-Harb, S., Harrus, I. M., Petre, R., Pavlov, G. G., Koptsevich, A. B., & Sanwal, D. 2001, *ApJ*, 561, 308
- Sankrit, R., & Hester, J. J. 1997, *ApJ*, 491, 796
- Shibata, S., Tomatsuri, H., Shimanuki, M., Saito, K., Nakamura, Y. & Mori, K. 2003, *MNRAS*, 346, 841
- Slane, P., Chen, Y., Schulz, N. S., Seward, F. D., Hughes, J. P., & Gaensler, B. M. 2000, *ApJ*, 533, L29
- Toor, A., & Seward, F. D. 1974, *AJ*, 79, 995
- Townsley, L. K., Broos, P. S., Chartas, G., Moskalenko, E., Nousek, J. A., & Pavlov, G. G. 2002, *Nuclear Instruments & Methods in Physics Research Section A*, 486, 716
- Weisskopf, M. C., Hester, J. J., Tennant, A. F., et al. 2000, *ApJ*, 536, L81
- Willingale, R., Aschenbach, B., Griffiths, R. G., Sembay, S., Warwick, R. S., Becker, W., Abbey, A. F., & Bonnet-Bidaud, J.-M. 2001, *A&A*, 365, 212
- Wise, M. W., Davis, J. E., Huenemoerder, Houck, J. C., Dewey, D., Flanagan, K. A., and Baluta, C. 1997, *The MARX 2.0 User Guide*, CXC Internal Document

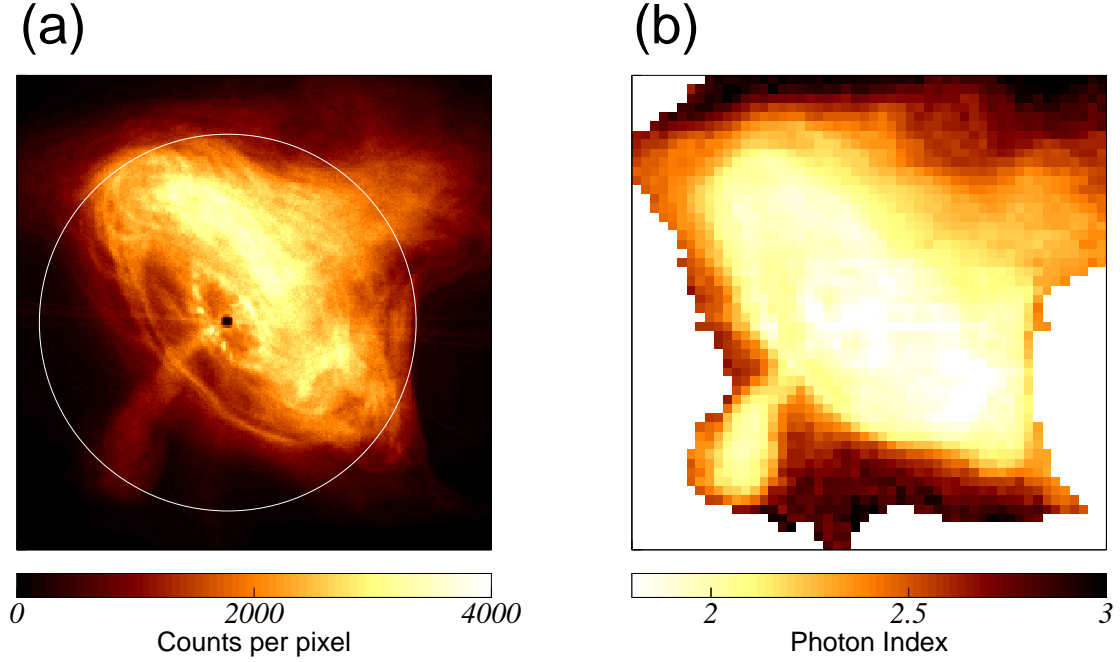


Fig. 1.— (a) *Chandra* ACIS-S combined image of the 2nd–8th observations. The center of the white circle ($R = 50''$) is located at the pulsar position. The “hole” at the pulsar position is caused by severe event pile-up resulting in the rejection of most events at this position. Narrow lines through the pulsar are instrumental artifacts due to trailing events. (b) Photon index map of the Crab Nebula after correction for pile-up effects. White regions around the eastern, western, and southern edges were excluded from analysis due to the dominance of trailing events and scattered photons. The pulsar position is also white because no photon index could be derived there due to severe pile-up.

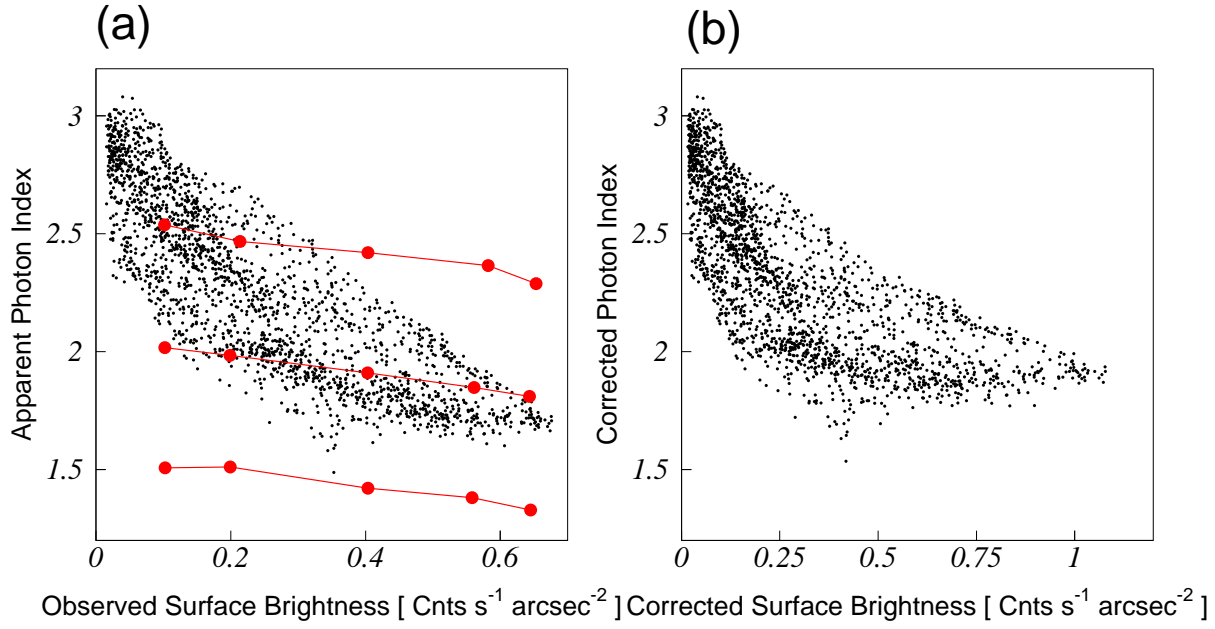


Fig. 2.— (a) Plot of apparent photon index against observed surface brightness derived from $2''.5 \times 2''.5$ square regions. Results of pile-up simulations for incident photon index of 1.5, 2.0, and 2.5 are superimposed (red lines), which shows that pile-up results in smaller photon index in higher surface brightness. (b) Same as (a) but corrected for pile-up effects.

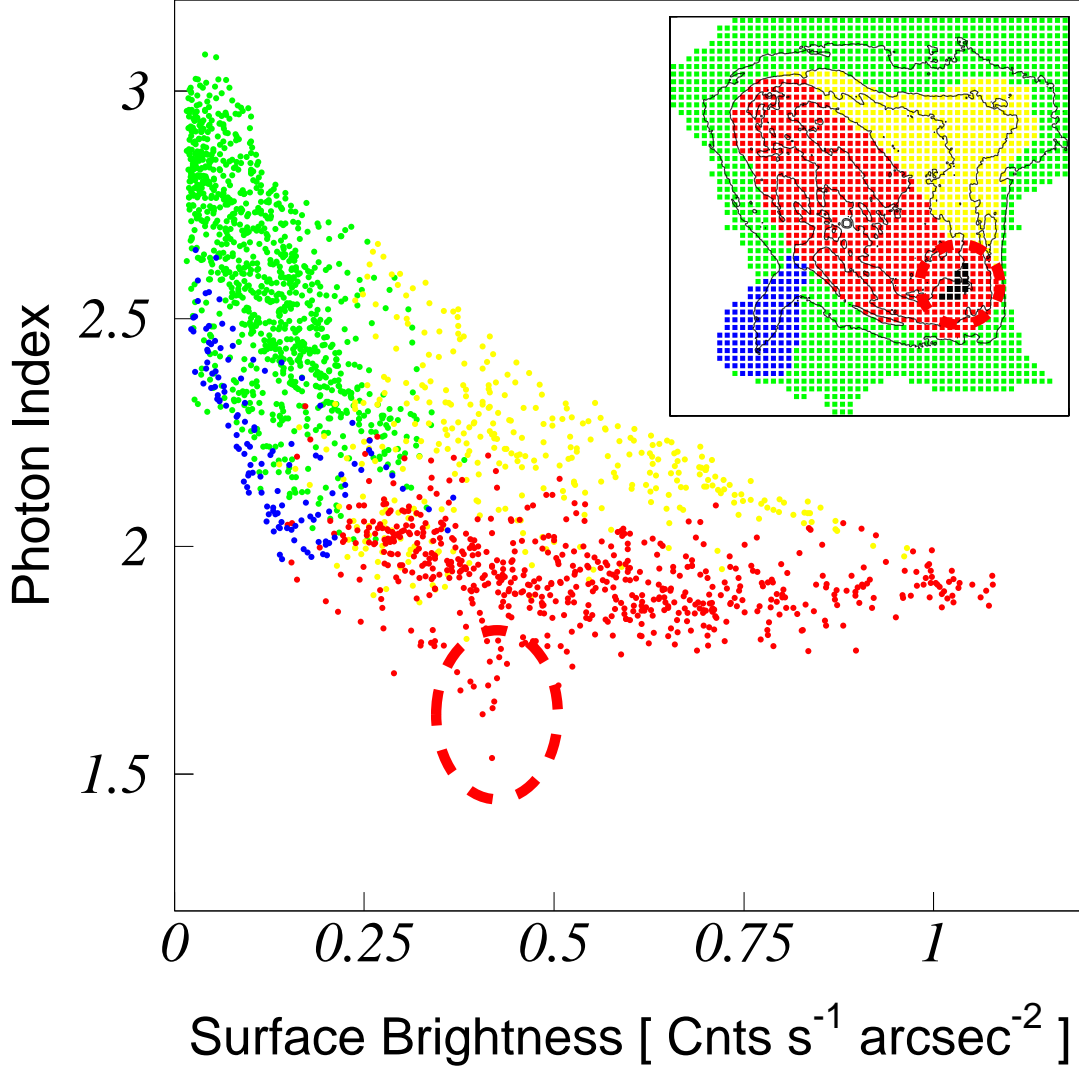


Fig. 3.— Plot of photon index against surface brightness, same as Figure 2b. The data points of the torus, the jet, the umbrella-shaped northwest region, and the faint peripheral region are color-coded as red, blue, yellow, and green, respectively. The inset shows the definitions of the four regions. The black contours represent surface brightness. The red dashed circle encloses data points with unusually small photon index compared to others (see §4.3). The corresponding positions in the nebula are shown in black in the inset, also enclosed by a red dashed circle.

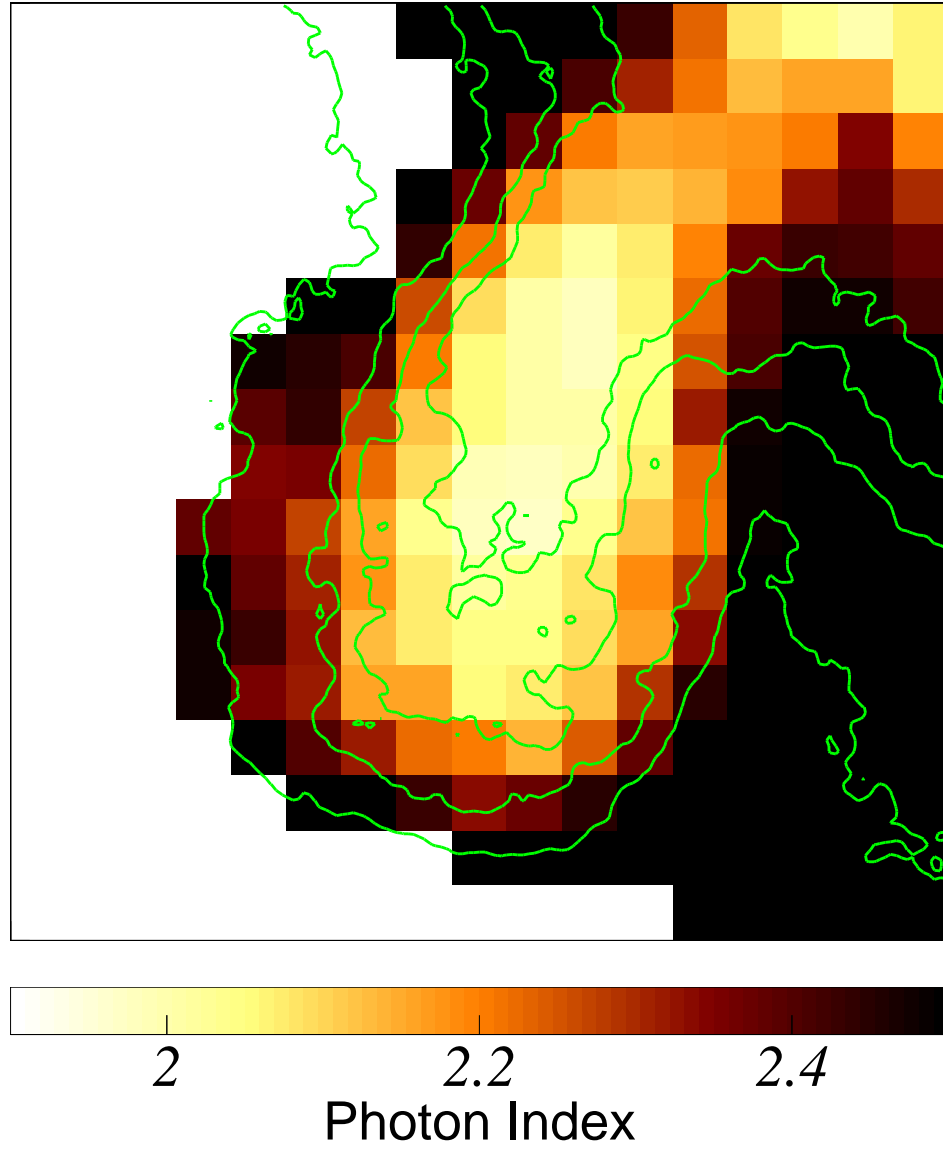


Fig. 4.— Close-up view of photon index map around the southern jet. Note that the range of photon index is different from that in Figure 1a to show fine variation. The green contours represent surface brightness.

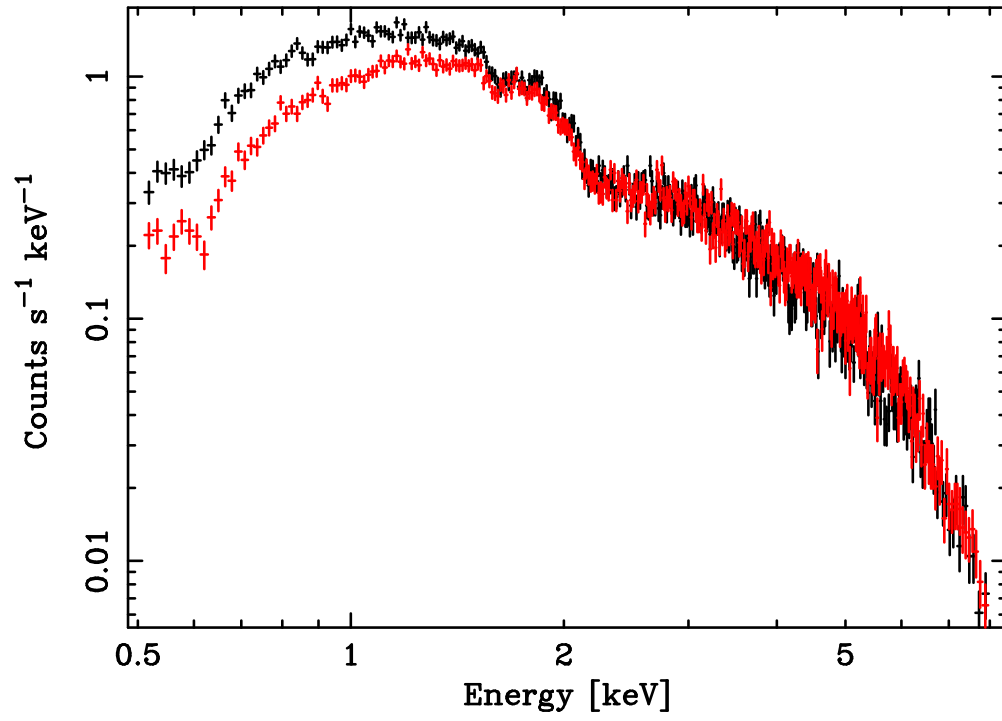


Fig. 5.— Spectra extracted from one of the small photon index regions (red) and a neighboring region (black).

Table 1. Observational log of the Crab Nebula

ObsID	Date	Coord.(J2000) ^a	Exposure (sec)
1994	3 November 2000	83.637, 22.024	3241.8
1996	25 November 2000	83.632, 22.014	2926.8
1998	18 December 2000	83.631, 22.016	2703.8
1999	9 January 2001	83.631, 22.017	2663.4
2001	30 January 2001	83.631, 22.017	2553.0
1995	21 February 2001	83.631, 22.017	2648.0
1997	14 March 2001	83.631, 22.017	2568.6
2000	6 April 2001	83.631, 22.016	2643.0

^acoordinates of the center of the subarray

Table 2. Spectral parameters for whole nebula

Parameter	Uncorrected Value	Corrected Value	Canonical Value
N_{H} (10^{22} cm^{-2})	0.27	0.32 (fixed)	0.33–0.36 ^a
Photon index	1.92	2.10	$2.10 \pm 0.03^{\text{b}}$
Normalization ^c	6.57	9.65	$9.7 \pm 0.5^{\text{d}}$

^aKuiper et al. (2001)

^bToor & Seward (1974)

^c(Photons $\text{cm}^{-2} \text{ s}^{-1} \text{ keV}^{-1}$ at 1 keV)

^dWillingale et al. (2001)